physica status solidi a
www.pss-a.com

Temperature-Dependent Operando Raman Analysis of a WO_3-Based Metal-Oxide Gas Sensor Detecting Triacetone Triperoxide

Johannes Warmer, Rene Breuch, Michael J. Schöning, Patrick Wagner, and Peter Kaul*

In this work, the surface reactions of the homemade explosive triacetone triperoxide on tungsten oxide (WO_3) sensor surfaces are studied to obtain detailed information about the chemical reactions taking place. Semiconductor gas sensors based on WO_3 nanopowders are therefore produced and characterized by scanning electron microscopy, X-ray diffraction, and Raman spectroscopy. To analyze the reaction mechanisms at the sensor surface, the sensor is monitored online under operation conditions using Raman spectroscopy, which allows to identify the temperature-dependent sensor reactions. By combining information from the Raman spectra with data on the changing resistivity of the underlying semiconductor, it is possible to establish a correlation between the adsorbed gas species and the physical properties of the WO_3 layer. In the results, it is indicated that a Lewis acid–base reaction is the most likely mechanism for the increase in resistance observed at temperatures below 150 °C. In the results, at higher temperatures, the assumption of a radical mechanism that causes a decrease in resistance is supported.

1. Introduction

Triacetone triperoxide (TATP) gained notoriety as an explosive in terrorist attacks over the last decades, e.g., in Madrid (2004), London (2005), Paris (2015), and Brussels (2016).[1] For the detection of TATP, some basic characteristics of the substance should be considered to find suitable approaches for sensors and procedures for bomb detection before a potential explosion. TATP is a crystalline, colorless substance without any characteristic UV–vis or fluorescence spectra.[2] In literature, the melting point is reported at 94 °C, but depending on the purity, TATP decomposes before reaching this temperature.[3] The predicted rate-determining step for thermal decomposition is the homolytic cleavage of the peroxide bond, which has an energy barrier of approximately 142–155 kJ mol^{-1} (34–37 kcal mol^{-1}).[2] Different studies were performed on the determination of the decomposition products of TATP.[2,4] For an explosive, the vapor pressure of TATP is already quite high at room temperature (RT), with 6.31 Pa at 25 °C.[5] TATP can be used as a main charge and as an ignition charge. Because of the easy availability of the educts (acetone, hydrogen peroxide, and an acid), TATP is often used in terroristic attacks. A variety of sensor systems was recently developed, based on different characteristic chemical and physical properties of the molecule, including quartz crystal microbalances,[6] fluorescence sensor systems,[7–9] solid membrane electrodes,[10] colorimetric sensors,[1,11] or thermodynamic sensors.[12] Furthermore, metal-oxide-semiconductor gas (MOX) sensors are also widely used to detect TATP and suitable metal oxides for this purpose are In_2O_3,[13] ZnO,[14] TiO_2,[15] SnO_2, and WO_3.[16] However, with the exception of the colorimetric sensor, which is commercially available, all of these sensors are in the stage of laboratory demonstrators and prototypes. As a result of the low stability, sensors are also being developed specifically for the detection of the reactants or decomposition products of TATP, such as solid-state fluorescence sensors[17] or MoS_2 with reduced graphene oxide (RGO) sensors.[18]

This publication is focusing on MOX sensors based on WO_3, a yellow metal oxide with a melting point of 1473 °C. At standard conditions, WO_3 has a ReO_3 structure, consisting of WO_6 octahedra that are connected along the edges in all three spatial dimensions.[19] WO_3 is a wide bandgap semiconductor with a

J. Warmer, R. Breuch, P. Kaul
Institute of Safety and Security Research
Hochschule Bonn-Rhein-Sieg University of Applied Sciences
Heisenbergstraße 16, D-53359 Rheinbach, Germany
E-mail: rene.breuch@dlr.de

R. Breuch
German Aerospace Center (DLR)
Institute for the Protection of Terrestrial Infrastructure
Rathausallee 12, D-53757 Sankt Augustin, Germany

M. J. Schöning
Institute of Nano- and Biotechnologies
Aachen University of Applied Sciences
Heinrich-Mussmann-Str. 1, D-52428 Jülich, Germany

P. Wagner
Laboratory for Soft Matter and Biophysics
Department of Physics and Astronomy
KU Leuven
Celestijnenlaan 200D, B-3001 Leuven, Belgium

The ORCID identification number(s) for the author(s) of this article can be found under https://doi.org/10.1002/pssa.202300790.

DOI: 10.1002/pssa.202300790

bandgap of 2.7 eV and additionally contains oxygen vacancies, which influence the electrical resistance.[20] These oxygen vacancies (V_O^*) act as an n-doping agent and increase the electronic conductivity according to the reaction Equation (1).

$$W_nO_{3n} \leftrightarrows W_nO_{3n-1} + V_O^* + e^- + \frac{1}{2}O_2 \quad (1)$$

In addition to pure tungsten oxide, different kinds of tungsten-based composite materials are used as gas sensors,[21] for example, C-doped WO_3 for the detection of acetone,[22] or doping with other metal oxides, such as Cr_2O_3.[23] Furthermore, polymorphic WO_3 in the form of nanopowders or nanowires is applied for improved NO_x detection.[24] NO_2 detection can also be enhanced with diverse WO_3 composites such as WO_3/RGO or with multiwall carbon nanotubes.[25]

Moreover, WO_3 is used as an electrochromic material in different coatings[26] or is applied as a catalyst in organic synthesis.[27] The studied attributes of tungsten oxide differ in acidity, the amount of tungsten surface atoms, and the carbon and hydrate surface species.[27–34] In summary, variety of reactions and interactions can take place at a WO_3 surface, which need to be considered when interpreting the surface reactions of TATP with WO_3.

In a previous study, we pointed out that WO_3-based sensors are able to detect TATP down to concentrations of a few parts per billion and, by using a temperature-cycling technique, we could increase the selectivity due to the dual behavior of the WO_3 sensors.[16] At temperatures below 150 °C, the electrical resistance increases due to TATP and, at higher temperatures, the resistance decreases upon exposure to TATP. A model for the surface reaction was designed based on the homolytic cleavage of the peroxide bond in the TATP molecule. This model describes an increase of resistance and acetone as degradation product at low temperatures, as well as the further reaction of the resulting acetone with the surface oxygen to CO_2, H_2O, and oxygen vacancies leading to a decrease of the sensors resistance at high temperatures.[16]

To analyze the chemical reactions on the sensor surface at these temperatures in depth, and to establish a reaction model, we have chosen operando Raman spectroscopy in the present work. The method of "operando" or "in situ" Raman spectroscopy has been used to analyze the behavior of metal-oxide gas sensors and catalysts as well as their adsorbed intermediates and decomposition products.[35] In this context, the Raman spectrum is recorded from the surface of an active gas sensor, e.g., ceria-based gas sensors,[36] indium oxide gas sensors,[37] and other metal-oxide gas sensors[38] or catalyst surfaces, like WO_3/TiO_2[39] or Mo–V–W–O catalysts,[40] while being exposed to an analyte such as ethanol[37] or educts, like NO_2[39] or propane.[40] In the present study, we produced both WO_3 and tin oxide (SnO_2) sensors by drop-casting of suspended nanopowders in water and characterized the sensor surface with X-ray diffraction (XRD), scanning electron microscopy (SEM) and Raman spectroscopy, including operando Raman experiments, to evaluate the surface chemistry in real time. Finally, the results will be interpreted and a possible mechanism for the temperature-dependent reactions of TATP at WO_3 surfaces will be proposed.

2. Experimental Section

In the following section, the materials and instrumentation as well as the analytical methods are explained and described in detail.

2.1. Gas Sensor Manufacturing

The MOX sensors used in this work were based on X34X substrates ($3 \times 3\,mm^2$ chip with $2 \times 1.4\,mm^2$ interdigitated electrode structure) by UST (Umweltsensortechnik GmbH, Germany). These substrates consisted of aluminum oxide with an integrated heater and an interdigitated electrode structure made of platinum. Two different types of sensors were produced for this work, one consisting of WO_3 and the other of SnO_2. The sensing layers were deposited by drop-casting a dispersion on the substrate mentioned earlier. The dispersion consisted of 10 mg WO_3 (Sigma Aldrich, nanopowder <100 nm average particle size) or SnO_2 (Sigma Aldrich, nanopowder <100 nm average particle size), 40 µL distilled water, and 10 µL 30% acetic acid (Sigma Aldrich). A volume of 0.5 µL of this dispersion was dropped onto the sensor substrates and dried at RT with subsequent sintering at 600 °C for 36 h in air. At the end of the process, the interdigitated structure of the substrate was evenly covered with a thick layer of metal oxide.

2.2. Morphological Sensor Characterization (XRD and SEM)

The characterization of the sensor surface was performed by using a SEM (Jeol JSM-7200F) at 5–15 kV acceleration voltage with a working distance of 6.1–7.9 mm at magnifications from 750× to 60 000×. The phase compositions of the sensor surface were analyzed by XRD (Bruker D8 with Cu K_α radiation, 50 kV detector Vantec-500 2D) at RT and at 300 °C.

2.3. Gas Mixing Unit

To control the gas phase above the sensor surface, a gas mixing unit was designed (**Figure 1**), consisting of three mass flow controllers (MFC) (Model 1179C MKS Instruments GmbH, Germany). A flow of synthetic air (20.5% O_2, 79.5% N_2, hydrocarbon free, Westfalen AG, Germany) was controlled up to a flow rate of 2 L min^{-1} (MFC 1). The humidity was adjusted by bubbling synthetic air through two flasks filled with ultrapure water (MFC 2). With the ratio of MFC 1 and MFC 2, the humidity could be adjusted between 5% and 95% relative humidity. MFC 3 was used to induce TATP into the gas stream by a flow of synthetic air through the flask filled with TATP, phlegmatized with sintered corundum, with a maximum flow of 20 mL min^{-1}. Details of phlegmatization are given in the work of Warmer et al.[16] For the reference measurements, the flask with phlegmatized TATP was replaced with a flask of acetic acid and acetone and measurements with the same flow of 20 mL min^{-1} were performed.

For the analysis of the gas phase, an infrared (IR) analysis was done with a gas-phase Fourier-transform infrared (FT-IR) spectroscopy spectrometer (Model CX4000 Gasmet Technologies GmbH, Germany). This spectrometer used a Peltier-cooled

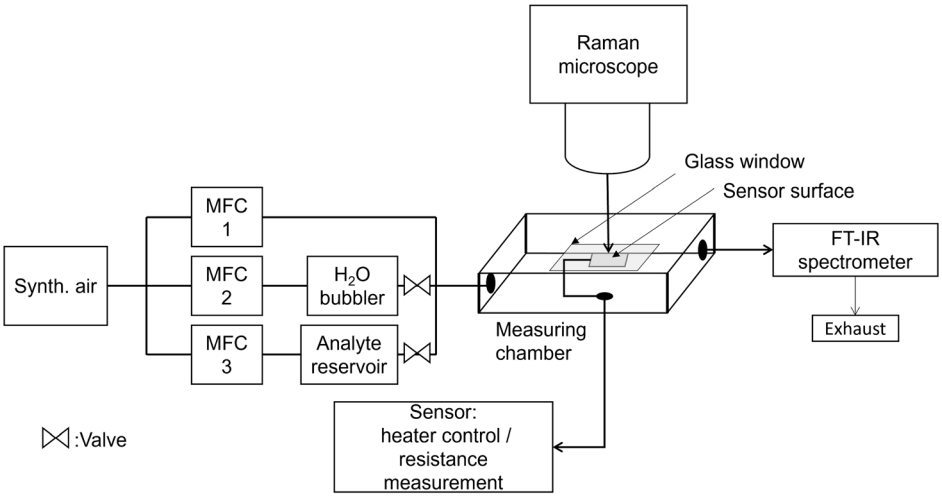

Figure 1. Schematic overview of the used gas exposure setup with gas mixing unit consisting of three mass flow controllers (MFC), the measuring chamber with a glass window, Raman microscope, IR spectrometer, and the electronic control unit for heating up the sensor and to measure the sensor resistance.

mercury cadmium telluride detector and a SiC-IR source. The gas phase was scanned with 10 scans s^{-1} in the wave-number range from 900 to 4200 cm^{-1}. All experiments were performed at 50% relative humidity with a total gas flow of 100 mL min^{-1}. The electrical resistance of the sensors was measured in two-point direct current (DC) mode with a Keithley 2700 digital multimeter.

2.4. Raman Microscopy

For the Raman analysis, the Raman microscope Senterra R200L from Bruker (Germany) was used. It consisted of the Olympus BX51 microscope and a Raman spectrometer. A laser with the wavelength $\lambda = 532$ nm and a maximum power of 20 mW was focused by a 20× objective (LMPlan FL N 20x, Olympus, Japan) with a numerical aperture of 0.4 and a working distance of 12 mm. A grating with 1200 lines mm^{-1} and an Andor Du420-OE detector with 2014×256 pixels were used to detect the Raman scattered light. During the analysis, the sensors were placed in a measuring chamber with a gas volume of 20 mL, with a sealed glass window at the upper side and a sealed electronic connection at the bottom. A photograph of the measuring chamber inside the Raman microscope is shown in Figure S1, Supporting Information.

Within this work, different parameters were used to record the Raman spectra. For the main operando investigations, the Raman spectra were recorded with the wavelength $\lambda = 532$ nm at 10 mW laser power, added up 800 times, each recorded over 0.8 s. For specific purposes, also other values for the laser power, collection time, and number of spectra were used within this study.

Due to the explosive character of crystalline TATP, the reference spectrum was recorded with $\lambda = 532$ nm at 2 mW, 60 spectra were added up, and each was collected over 1 s. For the comparison of the C–H vibrations of possible liquid decomposition products, the spectra were recorded with $\lambda = 532$ nm at 20 mW, and 15 spectra were added up, each one collected over 6 s. For the comparison of gaseous decompositions products on the active sensors with TATP, the spectra were recorded with $\lambda = 532$ nm at 10 mW, with 1 s integration time and with a sum of 500 times for RT measurements and 2000 times for measurements at 100 °C, respectively. Furthermore, the Raman spectrum of WO_3 with acetone at 100 °C was recorded with $\lambda = 532$ nm at 2 mW during 6 s and summed up over 50 repetitions.

For further analysis of the Raman data, we used a spectrum subtraction method as a post-processing method to generate so-called difference Raman spectra. For this, every operando Raman measurement was collected twice, in the presence of the analyte and without the analyte (background), for each temperature. After the spectra were added up for the actual measurement, also the background spectra were summed up, and both sum-spectra were subtracted from each other to generate the difference operando Raman spectra.

2.5. Temperature-Dependent Operando Experiments

To understand the reactions between TATP and WO_3, a temperature-dependent Raman study was performed. The differential Raman spectra of the WO_3 gas sensor were recorded at temperatures ranging from RT up to 350 °C while 12 ppm TATP was present in an air stream above the sensor. Each temperature was held for 6 h, the first 3 h without, the next 3 h with 12 ppm TATP in the gas stream. Between each temperature step, the sensor chamber was flushed with synthetic air and the sensor was heated up to 500 °C for 3 h to release possible residues and ensure a clean surface. The Raman spectra were recorded 800 times over 0.8 s (integration time for the recording of one spectrum) and then summed up (Bruker OPUS 7.5 software, co-addition) to obtain a high signal-to-noise ratio. Simultaneously, the electrical resistance of the sensor as well as the TATP concentration in the gas stream was analyzed by FT-IR. The sensor signal was calculated using Equation (2).

$$S_N = \frac{R_{TATP} - R_0}{R_0} \times 100\% \quad (2)$$

Here, S_N is the normalized signal, R_{TATP} is the averaged resistance over the last 5 min of every temperature step with TATP, and R_0 is the averaged resistance over the last 5 min of every temperature step without TATP.

To interpret the amount of surface-bound oxygen species in Section 3.3, the integration of the Raman peak centered around 1996 cm^{-1} was performed by Bruker OPUS 7.5 software, with linear background subtraction and the integration limits from 1870 to 2100 cm^{-1}.

$$PA_C = \frac{PA_{TATP} - PA_0}{PA_0} \times 100\% \quad (3)$$

Similar to the normalization of the resistive sensor data, the change in peak area (PA) centered around 1996 cm^{-1} was normalized using Equation (3) for a better comparison. Therefore, the PA for further evaluation is recorded while TATP is present in the air stream (PA_{TATP}), and without TATP (PA_0).

2.6. TATP Synthesis and Used Chemicals

TATP was prepared following the synthesis route of Matyás et al.[41] Sulfuric acid (Merck) was used as a catalyst. For the synthesis of TATP, a molar ratio between acid (31% H_2SO_4) and acetone (Optigrade HPLC, 99.5%, Promochem, Germany) of 0.5 was used. Detailed information on our synthesis protocol and phlegmatization is given in previous work.[16] As reference substances for a spectral comparison of the C–H vibrations, methanol, ethanol, isopropanol, acetone, formaldehyde, acetic acid, methyl acetate, and ethyl acetate (all substances obtained from Sigma Aldrich, purity >99.8%) were used. This selection was made because of the known degradation products of TATP based on literature data.[2,4] The synthesized TATP was confirmed by the Raman und IR spectra in Figure S2, Supporting Information.

3. Results

3.1. Sensor Characterization

To characterize the surface morphology of WO_3, SEM was used, see **Figure 2**. The SEM image (left) shows agglomerated particles with diameters of ≈5–30 µm. Due to its nanoscaled raw material and low sinter temperature, the surface structure of the agglomerated particles can still be considered as nanoscaled (50–200 nm), which causes a high surface area (Figure 2, right side). The X-ray diffractogram of the sensor in 2θ Bragg–Brentano geometry, see **Figure 3**, shows tungsten oxide in its monoclinic phase structure. The interference peaks are caused by the sensor substrate (Al_2O_3) and the interdigitated structure of the electrodes (platinum).

To rule out that the sensor behavior at low (RT) and high temperatures (300 °C), described in our previous work,[16] is caused by a phase transition of WO_3 from the monoclinic to an orthorhombic structure,[29] the same sensor was heated up to 300 °C and measured again. In literature, the phase transition should occur at 330 °C, however, due to impurities of the material and the resistive heating setup of the UST sensor substrate, it could not be excluded that a phase transition occurs within the operating conditions in this experiment. No significant changes in the phase composition were observed and, therefore, we excluded this as a possible reason for the different sensor behavior at low and high temperatures.

3.2. TATP Adsorption on a WO_3-Coated Sensor

In **Figure 4**, the Raman spectra of a WO_3-based sensor are displayed at RT in a 100 mL min^{-1} gas stream of synthetic air with (black line) and without (red line) 12 ppm TATP. Tungsten oxide has an intense Raman spectrum with several peaks in the range below 1000 cm^{-1}, and all peaks are listed in **Table 1**. The spectrum is dominated by two peaks at 808 cm^{-1} (vibration of the O–WO bond in the monoclinic phase) and at 717 cm^{-1} (vibration of W–O bond). Above 1000 cm^{-1}, the intensity of the spectrum drops significantly, while peaks at 1161, 1396, and 1996 cm^{-1} are still detectable. The addition of TATP showed no noticeable effect on the spectrum below 1000 cm^{-1}. Above 1000 cm^{-1}, the addition affects the peak at 1996 cm^{-1} (W=O overtone) and new peaks around 3000 cm^{-1} (ν–C–H vibrations) emerge.

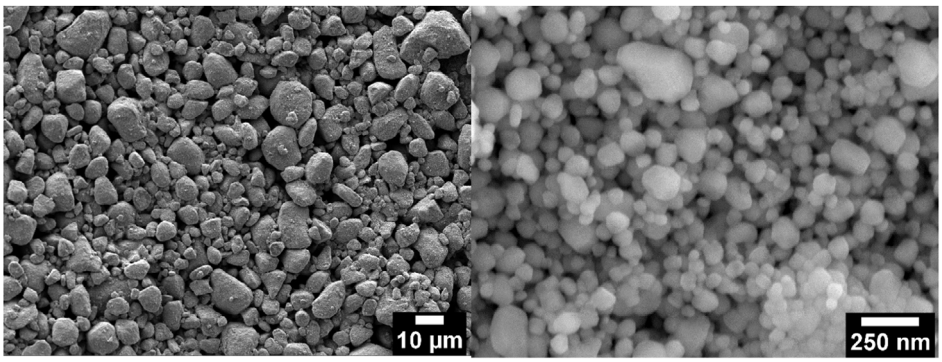

Figure 2. SEM image of a WO_3 sensor surface, at a magnification of 750× with 5 kV acceleration voltage and a working distance of 7.9 mm (left), and at a magnification of 60.000× with 15 kV acceleration voltage and a working distance of 6.0 mm (right).

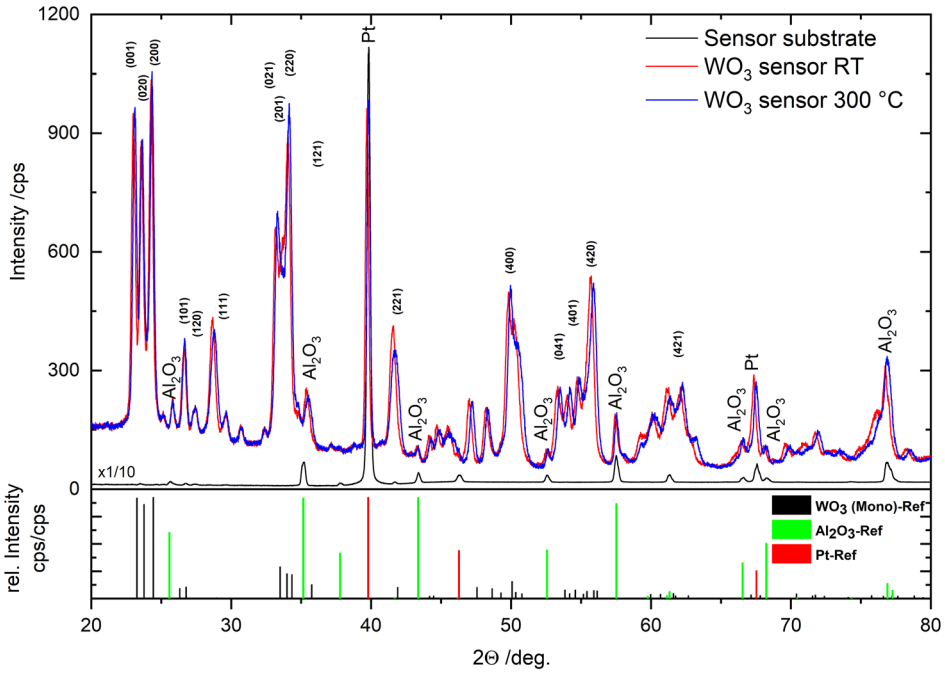

Figure 3. Upper part: XRD spectra of an empty sensor substrate consisting of Al_2O_3 with Pt electrodes (black line), and a WO_3 sensor at RT (red line) and 300 °C (blue line), respectively. Lower part: library reflexes of monoclinic WO_3 (black), Al_2O_3 (green), and platinum (red) references from Crystallography Open Database (COD).[55]

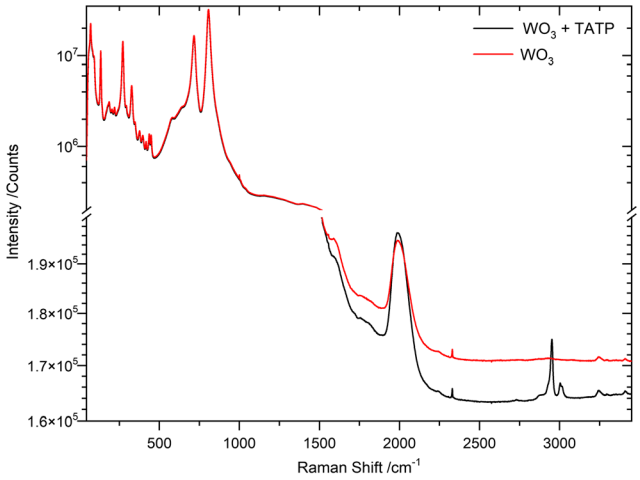

Figure 4. Raman spectra of a WO_3-based sensor at RT with (black) and without (red) 12 ppm TATP. The diagram has a split y axis, the upper part is in logarithmic scale, the lower part of the graph gives a more detailed, and linear-scaled view of the C–H vibrations, caused by organic adsorbates in the Raman spectrum (around 3000 cm^{-1}).

To analyze these peaks caused by TATP at 3000 cm^{-1} in detail, and to be able to detect more peaks caused by the addition of TATP (which may be covered by the intense WO_3 spectra), we focused on the difference spectra. Therefore, a spectrum of the sensor surface with TATP and the background spectrum without TATP were recorded at the same position on the sensor. Afterward, the background spectrum was subtracted from the spectrum with TATP, the resulting difference spectra are shown in **Figure 5**. Thereby, Figure 5a illustrates a normal Raman spectrum of crystalline TATP as a reference, Figure 5b,c illustrates different Raman spectra for a SnO_2-based sensor (as a metal-oxide reference without an intense Raman spectrum) and for a WO_3-based sensor, respectively.

The comparison between the Raman spectrum of crystalline TATP (Figure 5a) and the different Raman spectra of the SnO_2 sensor (Figure 5b) shows a good agreement. Nonetheless, several peaks in the range between 800 and 1000 cm^{-1} have a deformation in peak symmetry and lower relative intensity. These peaks are caused by vibrations of the peroxide bonds belonging to TATP;[42] it can be assumed that the TATP molecule is still in its ring form adsorbed at the surface. The double peak above 3000 cm^{-1} shows a similar deformation in symmetry and a lower relative intensity, both caused by the adsorbed TATP.[43] The WO_3-based sensor has a more intense spectrum than the SnO_2-based sensor: due to this, only the peaks in the area of 3000 cm^{-1} are recognizable, similar to the peaks of the crystalline TATP spectrum. The intense Raman spectrum of WO_3 (see Figure 4) complicated the generation of a difference Raman spectrum. In addition, it is noticeable that the overtone of the stretching ν (W=O) vibration at 1996 cm^{-1} is slightly increased in the difference Raman spectrum.

3.3. Temperature-Dependent Raman Studies

In the next experiments, the spectrum subtraction method was investigated in more detail for the WO_3 sensor. However, because of the intense spectrum of WO_3, the method was only

Table 1. Overview of the Raman data obtained within this work on WO_3, comparison to literature, and assignment of the peaks to specific vibration modes.

This work Raman peak [cm^{-1}]	Literature Raman peak [cm^{-1}]	Literature IR peak [cm^{-1}]	Description	Literature
71.5	71	–	Low-frequency phonon temperature change marker lattice modes	[24,47,48]
134.5	134–136	–	Low-frequency phonon temperature change marker	[24,47,48]
187	187	–	Low-frequency phonon temperature change marker	[24,47,48]
204.5	205	–	–	[47]
220.5	220–221	–	W–W	[24,47]
273	273	275	δ(O–W–O) in monoclinic structure	[24,47–49]
293.5	294	–	–	[47]
327.5	326–328	330	δ(O–W–O)	[24,47,48]
348	348	–	–	[47]
377	376–378	–	δ(O–W–O)	[24,47]
399	397	–	–	[47]
437	434–437	–	WO_2W:W group bridged vibrations	[24,47,48]
578.5	576	–	–	[47]
642	639	–	–	[47]
717	715	–	ν (W–O)	[24,47,48]
807.5	807–808	–	ν (O–WO) monoclinic phase	[24,47]
–	–	948	ν (W=O)	[48]
–	1012–1016	–	W=O	[39]
1161	–	1156	W–O–H	[56]
1396.5	–	–	–	–
1996	–	2009	W=O overtone	[46]
1996	–	1950–2050	W=O overtone	[39]

used in the range between 2800 and 3150 cm^{-1} (C–H stretching vibrations). The sensor was heated up to different temperatures between RT and 150 °C and the difference spectra are shown in **Figure 6**. The related sensor responses are depicted in Figure S3 together with the IR monitoring data for TATP.

The increasing temperature has a significant influence on the spectra due to the increase in the desorption of TATP,[3] the beginning of degradation processes,[2,4] and the Raman excitation itself.[44] The intensities of the peaks around 3000 cm^{-1}, which can be assigned to the C–H vibration of TATP,[44,45] are only visible at 25 and 50 °C, and disappear completely at higher temperatures. The typical C–H stretching vibrations of TATP vanished completely at 100 °C. Only a peak at 2930 cm^{-1}, which interferes with the more intense peak at 2952 cm^{-1} at RT, did not decrease in intensity in the same way and was visible up to 150 °C. The interpretation and identification of these peaks are given in Section 3.4.

The change in sensor resistance caused by the presence of TATP during the recording of the temperature-dependent spectra can be seen in **Figure 7**, as well as the change in PA of the WO_3 peak at 1996 cm^{-1} (W=O overtone) within the temperature range from RT up to 350 °C.

At RT, the addition of TATP already resulted in a change of resistance. The maximum change of resistance was found at 75 °C. Above this temperature, the change in resistance decreased, and above 250 °C, the resistance change became negative. Below 200 °C, the change in the PA caused by TATP was positive with a maximum at 100 °C. At higher temperatures, the PA decreased up to 350 °C, where the average change in PA was close to zero. The temperature profile of the change in resistance and the change in PA at 1996 cm^{-1} shown here seem to be directly related to the oxidative character of TATP. This will be discussed in detail in Section 4.1.

3.4. Identification of Decomposition Products at Low Temperatures

To identify the decomposition product, which explains the peak at 2930 cm^{-1}, different organic substances known from literature as thermal decomposition products of TATP[2,4] were tested and their spectra are displayed in **Figure 8**. The following stable organic substances were analyzed: acetic acid as aqueous solution and as pure liquids, isopropanol, formaldehyde, methanol, ethanol, methyl acetate, ethyl acetate, and acetone.

Acetone and acetic acid provide the best matches with the peak of TATP on WO_3 at 100 °C in terms of peak symmetry and peak position, although the peak position of acetone and acetic acid is slightly shifted in their liquid forms, making them possible candidates for degradations products.

To have a closer look at the comparison, the spectra of TATP, acetone and acetic acid at the surface of the WO_3-based sensors at RT and at 100 °C are displayed in **Figure 9**.

The comparisons support the assumption that the peak shown in Figure 9b at 2930 cm^{-1} (red-dotted line (1)) is identical to the peak caused by acetone (Figure 9c), which was already present in the spectrum of WO_3 with TATP at RT as a shoulder peak. The peak caused by acetic acid at 100 °C (Figure 9d) does not fit, so acetic acid can be excluded as a possible candidate for a main decomposition product of TATP. The differences in the basic intensity are due to different Raman parameters (see caption of Figure 9). Since in this comparison it is not the intensity of the signal that is decisive, but its position, parameters had to be selected that allow a comparison of the position and are not distorted by signals that are too high (acetone) or too low (TATP).

4. Discussion

XRD measurements and Raman spectra both confirm the presence of crystalline WO_3 on the sensor substrate. SEM images display a highly structured surface, which results in a high effective surface area. This is beneficial to ensure that large amounts

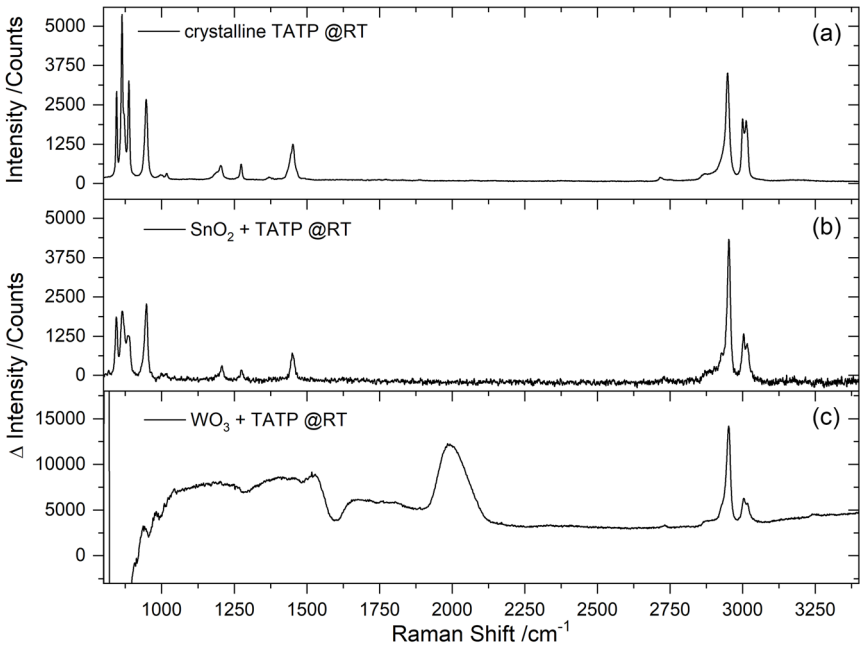

Figure 5. a) Reference Raman spectrum of crystalline TATP, b) different Raman spectra of a SnO_2-based sensor and c) a WO_3-based sensor. Both Raman spectra of the sensors are recorded at RT in synthetic air with 12 ppm TATP.

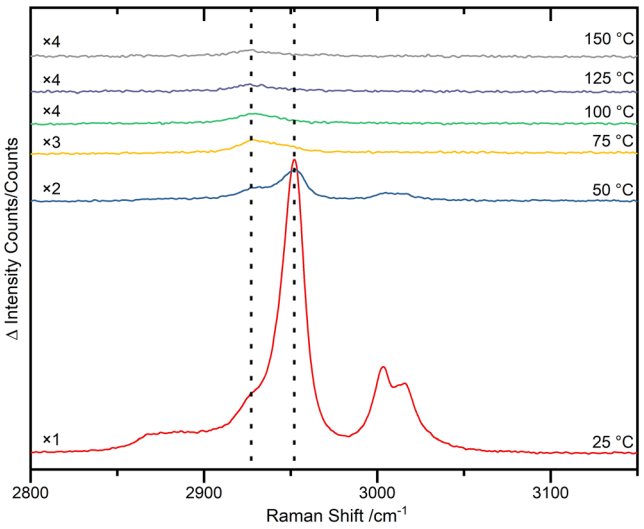

Figure 6. Difference spectra of a WO_3-based sensor with TATP in the C–H vibration range between 2800 and 3150 cm^{-1} at different sensor temperatures from RT to 150 °C. Magnification factors (left side) are added and shifted vertically for better visualization.

of TATP can adsorb on the WO_3, which enhances the sensor performance and eases the analysis of the reaction on the surface. Most of the WO_3 Raman peaks could be assigned to the vibrations documented in Table 1.

The Raman data in Figure 4 show that the addition of TATP to the gas stream has an influence on the WO_3 peak at 1996 cm^{-1}, which can be assigned to the overtone vibration of the WO_3 double-bound oxygen surface species, known in the IR and Raman spectrum of WO_3.[39,46] The TATP addition also resulted in new peaks at around 3000 cm^{-1}, that are similar to the peaks of TATP. The comparison in Figure 5 reveals multiple matches between the peaks and the crystalline TATP reference. In contrast to the bulk material, the deformation in peak symmetry and the relative intensity has been explained by the adsorbed species of the target molecule on the surface. This was already noticed for several other molecular species (H_2O/D_2O, acetone, proteins) on WO_3 and other metal-oxide surfaces.[47–49] This observation also holds for the similarly observed peak deformation of TATP in contact with SnO_2 surfaces, see Figure 5.

It is possible that the different peak symmetry and intensity are caused by a change in the environment around the TATP molecule because of the adsorption and the resulting inhibition of certain vibrations. The nearly same changes in peak symmetry and intensity at the peaks around 3000 cm^{-1} were noticeable for TATP measurements on the tin oxide surface. Nonetheless, the peaks of the peroxide vibrations (around 800–1000 cm^{-1}) could still be detected on the tin oxide surface, which leads to the interpretation that at RT, the ring structure of the major amount of the observed TATP on tin oxide and tungsten oxide was still intact and not decomposed.

With the major amount of TATP still intact, a closer look on the peak at 2930 cm^{-1} can lead to the assumption, that at RT a small amount of TATP decomposed. This suggestion is strengthened by temperature-dependent measurements where the peak at 2930 cm^{-1} does not decrease in the same way as the peaks of the TATP spectrum; instead, it stays observable up to a sensor temperature of 150 °C. The intensity decrease of the TATP spectrum can be explained by an increasing desorption rate of TATP at higher temperatures and the beginning of decomposition, which normally starts before reaching the melting point of 94 °C. In addition to the changing peaks in the area around

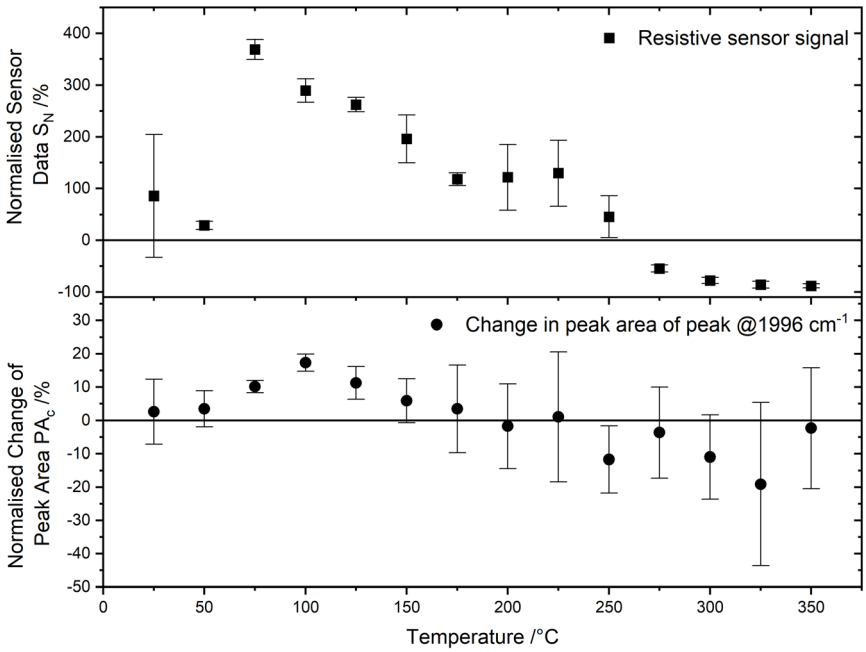

Figure 7. Temperature-dependent behavior of the resistive sensor signal (upper diagram) and the peak area of the WO_3 Raman peak at 1996 cm^{-1} (lower diagram). Both data sets were taken during the exposure to 12 ppm TATP in the temperature range between RT and 350 °C. The experiment was repeated three times at different measuring points on the sensor surface. The data points correspond to the average values and the error bars represent the standard deviation.

3000 cm^{-1}, also the WO_3 peak at 1996 cm^{-1} changes its intensity through the addition of TATP, which may indicate oxidation of the WO_3 surface.

Through the small absolute mass (≈0.1 mg) of WO_3 and the very small sensor surface compared to the gas volume, the decomposition conversion of TATP is quite small, so that no change in TATP concentration can be monitored by IR spectroscopy; however, the described change in the Raman spectrum can be used to identify the main decomposition product. By comparing the peaks around 3000 cm^{-1} (especially the 2930 cm^{-1} peak) with different organic alcohols, esters, ketones, and aldehydes, the best match seems to be acetone. In addition to the acetone peak, no evidence for other decomposition products could be found at low temperatures. This indicates that acetone and the increased amount of W=O double bonds are the decomposition products at low sensor temperatures.

4.1. Reaction-Scheme Model

With this new evidence, identification of acetone as main reaction product and the change of the amount of double-bound oxygen as surface species are correlated with the resistance change of the sensor. Thereby the former theoretical model for TATP detection with WO_3-based MOX sensors can be extended to the oxidative sensor reaction at low temperatures.[16] At higher temperatures (300 °C), the theory seems to be correct. The high temperature results in a thermal and radical decomposition starting with a homolytic cleavage of the peroxide bond of the TATP molecule, which leads to many decomposition products that are oxidized by the high temperature of the sensor, increasing the amount of vacancies and decreasing the electrical resistance.[16] At low temperatures, the theory was also based on a radical mechanism (see Section 1, Introduction), which also leads to acetone and an oxidation of the WO_3 surface, resulting in an increasing sensor resistance. The new findings of our present work improve the old theory and clear up some observations and suggestions: in case of a radical decomposition of TATP, other by-products should be detectable in the Raman analysis, due to the high reactivity of radicals.[50] In our work, however, only acetone as the single decomposition product could be determined at low temperature, which contradicts a radical mechanism for this temperature range. To find an alternative reaction mechanism for low temperatures, a closer look at the reactivity of the system is necessary. In literature, different reaction mechanisms for metal-oxide gas sensors in general, and in particular for the combination of tungsten oxide with TATP, are reported: adsorbed oxygen species,[51] oxygen vacancies,[35] adsorption of an analyte molecule,[52] formation of catalytic filamentous carbon (CFC),[30] Lewis-active sites,[53] Brønstedt-active sites,[53] and thermal decomposition of TATP.[2]

An accepted explanation for the functionality of metal-oxide gas sensors is related to a change in the amount of chemisorbed oxygen species at the metal-oxide surface, such as O^-, O_2^-, and O^{2-}, formed from atmospheric oxygen and electrons released from the conduction band (CB). A higher amount of oxygen species results in a higher electrical resistance. A second explanation is related to a change in the amount of oxygen vacancies and a lower amount of vacancies resulting in a higher electrical resistance.[54] With the results shown in Figure 7, either the amount of oxygen surface species increased, or the amount of oxygen

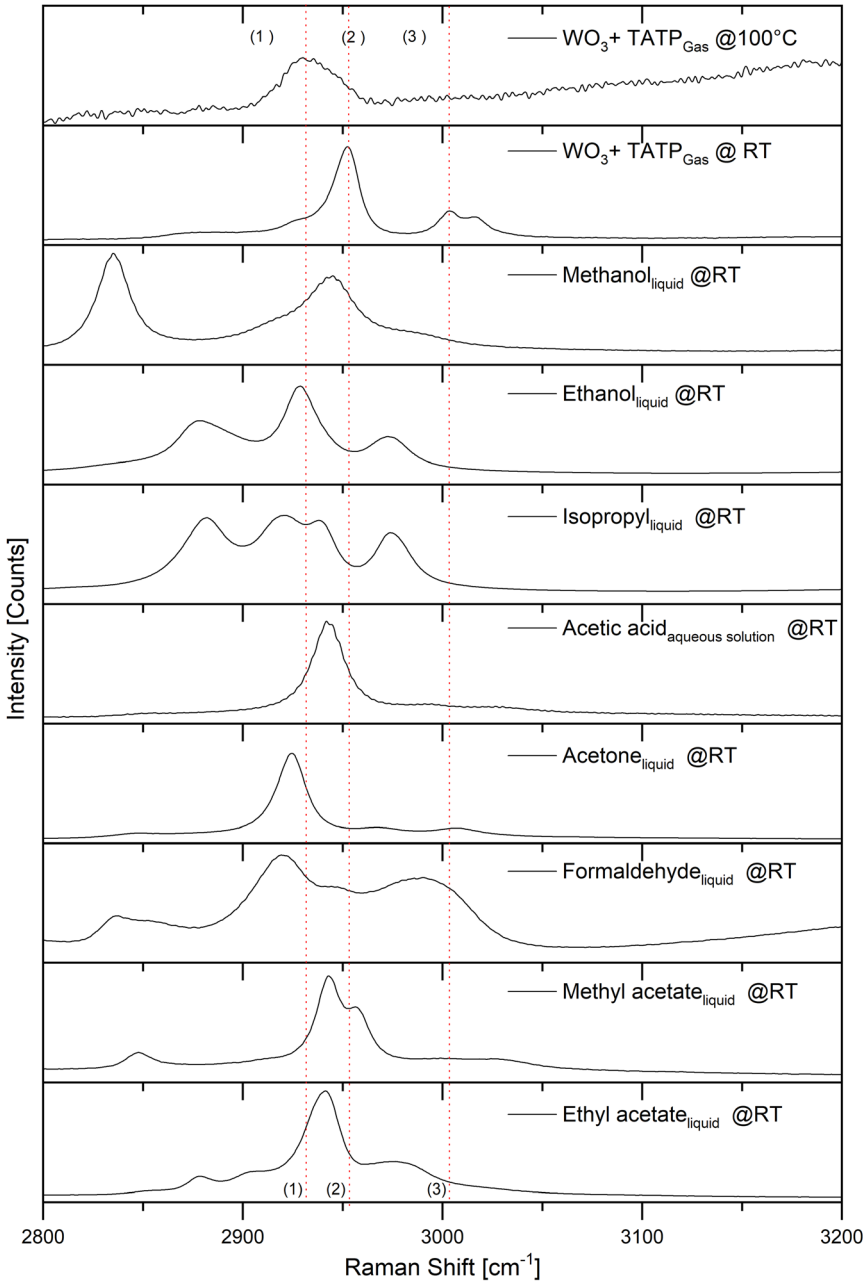

Figure 8. Comparison of Raman spectra in the range from 2800 to 3200 cm^{-1} of WO_3 with TATP in the gas phase at 100 °C and RT, and acetic acid as aqueous solution as well as isopropanol, formaldehyde, methanol, ethanol, methyl acetate, ethyl acetate, and acetone as pure liquids. Line (1) marks the C–H vibration of the dominant degradation species. Lines (2) and (3) mark the C–H vibrations of TATP. Possible candidates for the degradation products are acetone and acetic acid.

vacancies decreased with the addition of TATP to the gas stream and this should be considered in the reaction scheme. In the following paragraph, we will explain the aforementioned reactions by means of examples and finally compare them with possible reactions of the TATP at the WO_3 surface.

As an example for both oxygen vacancies and oxygen surface species, oxidizing species, like O_3, can act as reaction partners according to Equation (4) and (5) well described in literature:[24,35,50,54]

$$W_nO_{3n,} + V_O^* + e^-_{(CB)} + O_{3\,(Gas)} \rightarrow W_nO_{3n} + O_{2\,(Gas)} \quad (4)$$

$$O_{3\,(Gas)} + e^-_{(CB)} \rightarrow O_{2(Gas)} + O^-_{(Ads)} \quad (5)$$

An adsorption of molecular TATP similar to water, see Equation (6), could also be a reason for the increase in resistance at low temperatures.[52]

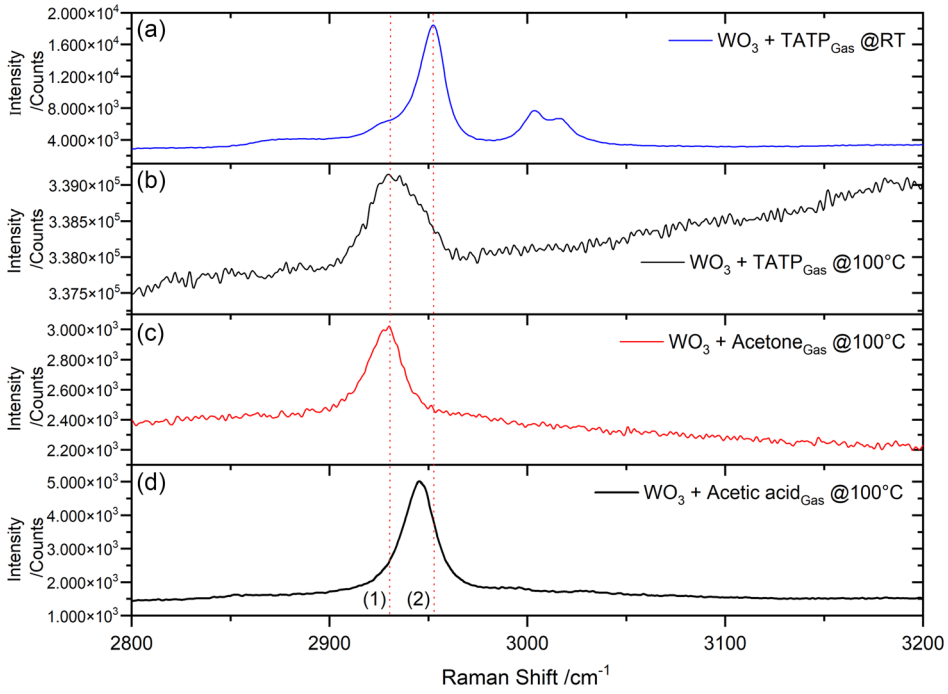

Figure 9. Raman spectra in the range from 2800 to 3200 cm^{-1} of the WO_3 sensor with a 100 mL min^{-1} gas stream with 12 ppm TATP at sensor temperatures of RT a) and 100 °C b). The spectra are recorded with a laser with the wavelength of 532 nm at 10 mW, with 1 s integration time and with a sum of 500 repetitions at RT and 2000 times at 100 °C. Furthermore, the Raman spectrum of WO_3 with acetone at 100 °C c) and with acetic acid at 100 °C d) is displayed, recorded with the same laser, but with 2 mW, 6 s and added up over 50 repetitions. The two marks (dotted lines) are at the positions: 1) 2930 cm^{-1} and 2) 2952 cm^{-1}.

$$H_2O_{Gas} \rightarrow H_2O_{Ads} \rightarrow H_2O_{Ads}^{\delta+} + \delta e' \quad (6)$$

In case that the adsorption of TATP is the only reason for the sensor response, the highest sensor signal should be expected for the lowest temperature, here at RT. The results of Figure 7 clearly indicate, however, that the strongest resistance change occurs at 75 °C.

The formation of CFC on the surface of tungsten oxide nanoparticles up to 30 nm is also reported.[30] This CFC should have a major role in terms of its reactivity to oxidizing gases such as NO_2.[30] Nevertheless, we can rule out this possibility because we found no indications for CFC in the Raman spectra and no fibers in the SEM images, and also the particle size of WO_3 was larger than 30 nm as determined by SEM (Figure 2).

Furthermore, tungsten oxide is known as a strong Lewis (Equation (7)) and Brønsted acid (Equation (8)),[27] so that acid–base reactions between tungsten oxide and TATP are also possible, similar to the reaction with NH_3 in the following equations.[53]

$$W + |NH_{3Gas} \rightleftharpoons W - NH_3 \quad (7)$$

$$W - OH + |NH_{3Gas} \rightleftharpoons W - O^- + NH_4^+ \quad (8)$$

A Brønstedt acid–base reaction between WO_3 and TATP would result in a protonated TATP molecule, which could lead to rapid decomposition, due to the remaining oxygen radical of the peroxide group. This process should then lead to the formation of alcohols, carboxylic acids, or esters. However, no evidence

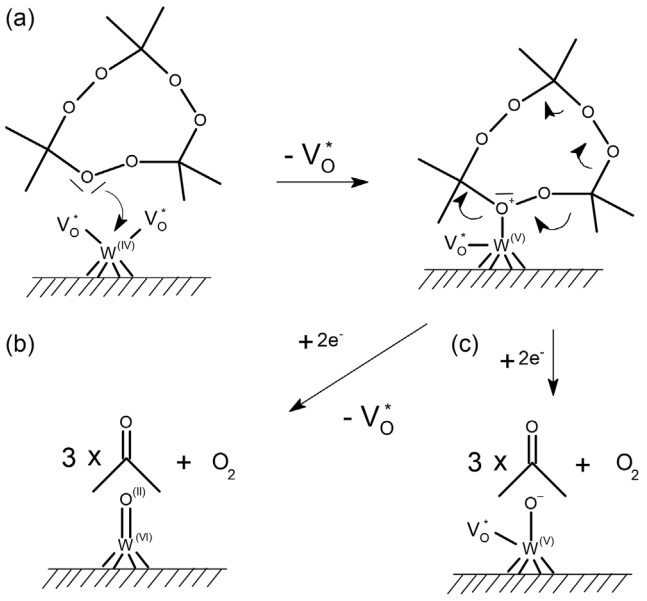

Figure 10. Possible reaction scheme for the sensor reaction at low sensor temperature. a) Due to the Lewis acid–base reaction, TATP gets a positive charge, which destabilizes the molecule and consumes an oxygen vacancy V_O^*. b) The rapid decomposition of TATP (valence shifting marked with arrows) can either consume two electrons and another V_O^*, furthermore resulting in an increase of the valence state of tungsten or c) just two electrons, leading to three molecules of acetone, one molecule oxygen and either a tungsten oxygen double bond or a negatively charged oxygen surface species.

of such decomposition product could be found. Thus, the Lewis acid–base reaction seems to be a plausible mechanism for the low-temperature sensor signal.

In a Lewis acid–base scenario, a nonstoichiometric tungsten oxide site would react with TATP, consuming an oxygen vacancy und inducing a positive charge into the TATP molecule. This is illustrated in **Figure 10**, reaction scheme (a). The positive charge will then destabilize the TATP molecule, resulting in the rapid decomposition into molecular oxygen and three molecules of acetone. During this decomposition, either another vacancy and two electrons from the CB are consumed, forming a tungsten-oxygen double bond (Figure 10, reaction b), or only two electrons are consumed, forming an adsorbed oxygen species (Figure 10, reaction c).

Both pathways as shown in Figure 10b,c explain the increase of resistance and the high amount of acetone found by the Raman spectroscopy together. The reaction (b) of Figure 10 can also explain the increase of the Raman peak at 1996 cm^{-1} caused by TATP, making this mechanism favorable for the reaction mechanism at low sensor temperature.

5. Summary and Conclusions

In conclusion, we have prepared drop-casted polycrystalline WO_3-based gas sensors with a large active surface for the detection of TATP. An operando Raman setup was constructed and used to study the reaction between TATP and tungsten oxide. Thereby, characteristic Raman peaks of the C–H groups of adsorbed TATP were detected at RT on the tungsten oxide surface as well as a change in the peak intensity of a W=O double-band vibration. The temperature-dependent changes of the Raman peaks for C–H and W=O as well as the sensor behavior were analyzed, leading to two different reaction pathways. Below 200 °C, the Lewis acid–base reaction dominates, while above 200 °C the radical reaction dominates. For the sensor reaction at low temperatures, a comparison of the Raman signal was used to identify acetone as a stable decomposition product. Based on these findings, suggestions for different reaction schemes were discussed, leading to a Lewis acid–base reaction as the most likely reaction mechanism at low temperatures. Toward higher temperatures, the reaction mechanism most probably changes to a more complex mechanism with a higher content of radical reactions, starting with the cleavage of the peroxide bond, which leads to more complex reaction products and degradation mechanisms.

Supporting Information

Supporting Information is available from the Wiley Online Library or from the author.

Acknowledgements

This work was funded by the Institute of Safety and Security Research of Bonn-Rhein-Sieg University of Applied Science. The authors would like to thank Prof. Dr. Hans-Willi Kling from Bergische Universität Wuppertal for his advice and supervision during the preparation of a supporting master's thesis for this research. The authors also thank Sarah Andreas, Nina Hermes and Jessica Reinmüller for their assistance with English language editing in this work as well as Philipp Gillemot for his help with the XRD measurements.

Conflict of Interest

The authors declare no conflict of interest.

Data Availability Statement

The data that support the findings of this study are available from the corresponding author upon reasonable request.

Keywords

metal-oxide-semiconductor gas sensors, operando Raman spectroscopies, triacetone triperoxides, tungsten oxides

Received: October 12, 2023
Revised: February 27, 2024
Published online:

[1] B. Gökdere, A. Üzer, S. Durmazel, E. Erçağ, R. Apak, *Talanta* **2019**, *202*, 402.
[2] F. Dubnikova, R. Kosloff, J. Almog, Y. Zeiri, R. Boese, H. Itzhaky, A. Alt, E. Keinan, *J. Am. Chem. Soc.* **2005**, *127*, 1146.
[3] J. Mbah, D. Knott, S. Steward, *Talanta* **2014**, *129*, 586.
[4] J. C. Oxley, J. L. Smith, H. Chen, *Propellants, Explos., Pyrotech.* **2002**, *27*, 209.
[5] R. G. Ewing, M. J. Waltman, D. A. Atkinson, J. W. Grate, P. J. Hotchkiss, *TrAC - Trends Anal. Chem.* **2013**, *42*, 35.
[6] D. Lubczyk, C. Siering, J. Lörgen, Z. B. Shifrina, K. Müllen, S. R. Waldvogel, *Sens. Actuators, B* **2010**, *143*, 561.
[7] Y. An, X. Xu, K. Liu, X. An, C. Shang, G. Wang, T. Liu, H. Li, H. Peng, Y. Fang, *Chem. Commun.* **2019**, *55*, 941.
[8] A. Revilla-Cuesta, I. Abajo-Cuadrado, M. Medrano, M. M. Salgado, M. Avella, M. T. Rodríguez, J. García-Calvo, T. Torroba, *ACS Appl. Mater. Interfaces* **2023**, *15*, 32024.
[9] L. Zhang, L. Yang, J.-M. Han, *Sens. Actuators, B* **2023**, *385*, 133680.
[10] J. C. Mbah, S. Steward, N. O. Egiebor, *Sens. Actuators, B* **2016**, *222*, 693.
[11] H. Lin, K. S. Suslick, *J. Am. Chem. Soc.* **2010**, *132*, 15519.
[12] M. Amani, Y. Chu, K. L. Waterman, C. M. Hurley, M. J. Platek, O. J. Gregory, *Sens. Actuators, B* **2012**, *162*, 7.
[13] W.-H. Zhang, W.-D. Zhang, L.-Y. Chen, *Nanotechnology* **2010**, *21*, 315502.
[14] V. Dobrokhotov, L. Oakes, D. Sowell, A. Larin, J. Hall, A. Kengne, P. Bakharev, G. Corti, T. Cantrell, T. Prakash, J. Williams, D. N. McIlroy, *Sens. Actuators, B* **2012**, *168*, 138.
[15] R. S. Ray, B. Sarma, S. Mohanty, M. Misra, *Talanta* **2014**, *118*, 304.
[16] J. Warmer, P. Wagner, M. J. Schöning, P. Kaul, *Phys. Status Solidi A* **2015**, *212*, 1289.
[17] S. Fan, J. Lai, P. L. Burn, P. E. Shaw, *ACS Sens.* **2019**, *4*, 134.
[18] Q. Sun, Z. Wu, H. Duan, D. Jia, *Sensors* **2019**, *19*, 1281.
[19] A. F. Holleman, E. Wiberg, *Lehrbuch Der Anorganischen Chemie*, De Gruyter, Berlin **2008**.
[20] J. Guérin, K. Aguir, M. Bendahan, C. Lambert-Mauriat, *Sens. Actuators, B* **2005**, *104*, 289.
[21] G. Lei, C. Lou, X. Liu, J. Xie, Z. Li, W. Zheng, J. Zhang, *Sens. Actuators, B* **2021**, *341*, 129996.

[22] T. Xiao, X. Y. Wang, Z. H. Zhao, L. Li, L. Zhang, H. C. Yao, J. S. Wang, Z. J. Li, *Sens. Actuators, B* **2014**, *199*, 210.
[23] P. Gao, H. Ji, Y. Zhou, X. Li, *Thin Solid Films* **2012**, *520*, 3100.
[24] R. F. Garcia-Sanchez, T. Ahmido, D. Casimir, S. Baliga, P. Misra, *J. Phys. Chem. A* **2013**, *117*, 13825.
[25] U. Yaqoob, A. I. Uddin, G.-S. Chung, *Sens. Actuators, B* **2016**, *224*, 738.
[26] C. Li, J. H. Hsieh, M.-T. Hung, B. Q. Huang, *Thin Solid Films* **2015**, *587*, 75.
[27] J. Chauvin, K. Thomas, G. Clet, M. Houalla, *J. Phys. Chem. C* **2015**, *119*, 12345.
[28] W. Chu, Y. Ooka, Y. Kamiya, T. Okuhara, *Catal. Lett.* **2005**, *101*, 225.
[29] G. Busca, *Heterogeneous Catalytic Materials*, Elsevier, Amsterdam **2014**, pp. 103–195.
[30] M. Boulova, A. Gaskov, G. Lucazeau, *Sens. Actuators, B* **2001**, *81*, 99.
[31] I. E. Wachs, T. Kim, E. I. Ross, *Catal. Today* **2006**, *116*, 162.
[32] S. Du Kim, M. Ostromecki, I. E. Wachs, *J. Mol. Catal., A* **1996**, *106*, 93.
[33] Z. Zhang, J. Liu, J. Gu, L. Su, L. Cheng, *Energy Environ. Sci.* **2014**, *7*, 2535.
[34] D. Sudha, P. Sivakumar, *Chem. Eng. Process.* **2015**, *97*, 112.
[35] A. Gurlo, R. Riedel, *Angew. Chem., - Int. Ed.* **2007**, *46*, 3826.
[36] A.-K. Elger, J. Baranyai, K. Hofmann, C. Hess, *ACS Sens.* **2019**, *4*, 1497.
[37] S. Sänze, C. Hess, *J. Phys. Chem. C* **2014**, *118*, 25603.
[38] A.-K. Elger, C. Hess, *Sensors* **2019**, *19*, 5075.
[39] Y. He, M. E. Ford, M. Zhu, Q. Liu, Z. Wu, I. E. Wachs, *Appl. Catal., B* **2016**, *188*, 123.
[40] M. O. Guerrero-Pérez, M. C. Herrera, I. Malpartida, M. A. Larrubia, L. J. Alemany, M. A. Bañares, *Catal. Today* **2007**, *126*, 177.
[41] R. Matyáš, J. Pachman, *Propellants, Explos., Pyrotech.* **2010**, *35*, 31.
[42] R. J. Stokes, E. L. Normand, R. Lindley, P. Black, M. McCulloch, D. N. Middleton, W. E. Smith, B. Foulger, C. Lewis, in *Optics and Photonics for Counterterrorism and Crime Fighting V*, p. 74860O, https://doi.org/10.1117/12.830348.
[43] R. P. Cooney, G. Curthoys, N. T. Tam, *Adv. Catal.* **1975**, *24*, 293.
[44] G. Lucazeau, *J. Raman Spectrosc.* **2003**, *34*, 478.
[45] L. Jensen, P. M. Mortensen, R. Trane, P. Harris, R. W. Berg, *Appl. Spectrosc.* **2009**, *63*, 92.
[46] M. A. Vuurman, D. J. Stufkens, A. Oskam, G. Deo, I. E. Wachs, *J. Chem. Soc. Faraday Trans.* **1996**, *92*, 3259.
[47] E. Cazzanelli, C. Vinegoni, G. Mariotto, A. Kuzmin, J. Purans, *J. Solid State Chem.* **1999**, *143*, 24.
[48] M. F. Daniel, B. Desbat, J. C. Lassegues, B. Gerand, M. Figlarz, *J. Solid State Chem.* **1987**, *67*, 235.
[49] J. Pfeifer, C. Guifang, P. Tekula-Buxbaum, B. A. Kiss, M. Farkas-Jahnke, K. Vadasdi, *J. Solid State Chem.* **1995**, *119*, 90.
[50] *Van Nostrand's Scientific Encyclopedia*, https://doi.org/10.1002/0471743984.vse8264.
[51] G. Korotcenkov, V. Brinzari, B. K. Cho, *J. Sens.* **2016**, *2016*, 1.
[52] R. Pohle, M. Fleischer, H. Meixner, *Sens. Actuators, B* **2000**, *68*, 151.
[53] I. Jiménez, M. A. Centeno, R. Scotti, F. Morazzoni, J. Arbiol, A. Cornet, J. R. Morante, *J. Mater. Chem.* **2004**, *14*, 2412.
[54] V. Oison, L. Saadi, C. Lambert-Mauriat, R. Hayn, *Sens. Actuators, B* **2011**, *160*, 505.
[55] S. Gražulis, A. Daškevič, A. Merkys, D. Chateigner, L. Lutterotti, M. Quirós, N. R. Serebryanaya, P. Moeck, R. T. Downs, A. Le Bail, *Nucleic Acids Res.* **2012**, *40*, D420.
[56] C. J. Wright, *J. Solid State Chem.* **1977**, *20*, 89.